Transport Phenomena in Materials Processing

Transport Phenomena in Materials Processing

presented at

THE WINTER ANNUAL MEETING OF
THE AMERICAN SOCIETY OF MECHANICAL ENGINEERS
BOSTON, MASSACHUSETTS
NOVEMBER 13-18, 1983

sponsored by

COMMITTEE K-8, THE HEAT TRANSFER DIVISION
AND THE PRODUCTION ENGINEERING
DIVISION, ASME

edited by

MICHAEL M. CHEN, JYOTIRMOY MAZUMDER,
CHARLES L. TUCKER III
UNIVERSITY OF ILLINOIS AT
URBANA-CHAMPAIGN
URBANA, ILLINOIS

FOREWORD

Materials processing is the subject of transforming basic materials into useful objects by forming, joining and modification operations. Most materials processing operations involve transport phenomena: fluid flow, and transfer of heat, mass and momentum. Familiar examples are the solidification of a metal casting, or the flow of molten polymer into a mold. Less familiar examples are molecular diffusion and segregation during the solidification of multiphase alloys, and the rotary transport of reinforcing fibers during the molding of composites.

As a subject for research, materials processing is rich in many ways. It provides problems which are both intellectually challenging and of great practical significance. The papers in this volume demonstrate the variety of problems and solution techniques in this area. Also noteworthy is the diversity of background among the authors, who range from materials scientists to heat transfer and fluid flow specialists. Forums which bring this type of group together are important to the advancement of materials engineering.

The papers in this volume were presented at the Symposium on Transport Phenomena in Materials Processing at the 1983 Winter Annual Meeting of the American Society of Mechanical Engineers. We are grateful to the Heat Transfer Division and the Production Engineering Division for sponsoring the symposium, and hope that this is the first of many such gatherings.

<div style="text-align: right">

Michael M. Chen
Jyoti Mazumder
Charles L. Tucker III

University of Illinois
Urbana, Illinois

</div>

CONTENTS

NUMERICAL SOLUTIONS OF THERMOCAPILLARY FLOWS IN FLOATING ZONES

B-I. Fu and S. Ostrach

Department of Mechanical and Aerospace Engineering
Case Western Reserve University
Cleveland, Ohio

ABSTRACT

A finite difference scheme is used to determine the axisymmetric flow and temperature fields in a half floating-zone configuration. The primary purpose of this study is to determine the effects of the surface-tension Reynolds number, Marangoni number, and Prandtl number on the thermocapillary flow under weightless conditions. The range of parameters considered includes those for actual growth of silicon crystals. A strongly coupled nonlinear numerical scheme and variable grid size are utilized to obtain solutions at the appropriate large ranges of parameters.

The effects of buoyancy, surface heat loss, and aspect ratio are also investigated.

The flows are found to form essentially a single-cell pattern with the core located nearer to the free surface. The axial velocity near the free surface is two to four times larger than near the axis.

NOMENCLATURE AND GREEK SYMBOLS

A	Aspect ratio (L/R)
g	Gravity force
Gr	Grashof number $(\beta g \Delta\Theta L^3/\nu^2)$
h	Heat transfer coefficient from the melt to the air
k	Thermal conductivity of melt
L	Floating-zone length
Ma	Marangoni Number $(|\partial\gamma/\partial\Theta|\Delta\Theta R_0/\mu\nu)$
Nu	Nusselt number (hR_0/k)
Pr	Prandtl number (ν/α)
R	Radius coordinate
R_0	Radius of the floating zone

r	Dimensionless radius coordinate (R/R_0)
Re_s	Surface-tension Reynolds number (Ma/Pr)
T	Dimensionless temperature $(\Theta-\Theta_0)/\Delta\Theta$
U	Radial velocity
u	Dimensionless radial velocity (U/U^*)
U^*	Reference radial velocity $(\nu Re_s/L/A)$
W	Axial-velocity
W^*	Reference axial velocity $(\nu Re_s/L)$
z	Dimensionless axial coordinate (Z/L)
Z	Axial coordinate

Greek Symbols

α	Thermal diffusivity
β	Thermal expansion coefficient of melt
γ	Surface-tension
$\frac{\partial\gamma}{\partial\Theta}$	Surface-tension coefficient with respect to temperature
$\Delta\Theta$	Temperature difference between the top and bottom rods
Θ	Temperature variable
Θ_0	Bottom wall temperature
Θ_s	Surrounding temperature
μ	Dynamic viscosity
ν	Kinematic viscosity
ρ	Density of fluid

τ	Time
τ^*	Reference time ($L^2/\nu/Re_s$)
Ψ	Stream function
Ψ^*	Reference stream function ($\nu R_0^2 Re_s/L$)
ψ	Dimensionless stream function (Ψ/Ψ^*)
ω	Vorticity
ω^*	Reference vorticity ($\nu Re_s/L/R_0$)
Ω	Dimensionless vorticity (ω/ω^*)

INTRODUCTION

The floating-zone method has been widely adopted as a crystal growth process for high purity single crystals since the early 1950's. The advantage of this non-crucible process is that container contamination can be completely eliminated, [1] and [2]. The basic arrangement of floating-zone crystal growth is shown in Fig. 1. The top rod is a polycrystalline feed material, and the bottom rod is a pure single crystal. A melting zone is suspended between the top and bottom rods by surface-tension. The heat required for melting is supplied by an induction heating coil. Either the heating coil moves upward or the rods move downward to keep the single crystal growing continuously on the lower rod. Usually the top or the bottom crystal is rotated at a fixed speed. According to experience of the crystal growth industry, the rotation of the crystal can provide a uniform cylindrical crystal with better quality.
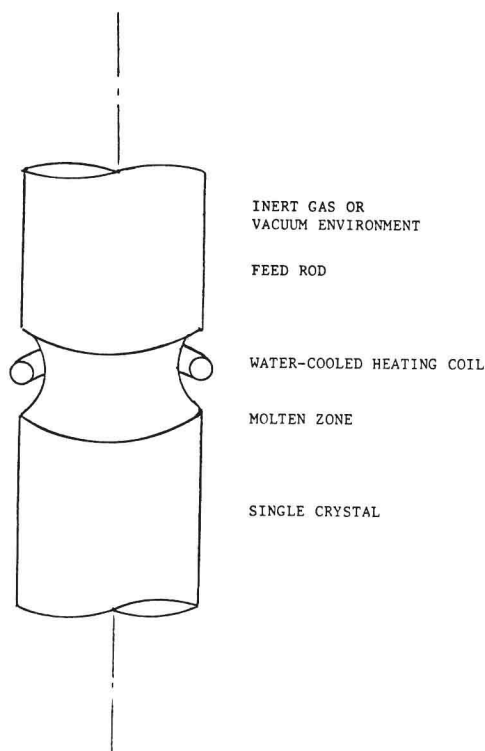

INERT GAS OR
VACUUM ENVIRONMENT

FEED ROD

WATER-COOLED HEATING COIL

MOLTEN ZONE

SINGLE CRYSTAL

Figure 1 Floating zone crystal growth

The size of the crystal grown by the floating-zone method is limited by the gravitational force, which over-whelms the surface-tension force as the diameter and zone length become large and causes the breakdown of the melting zone. The development of the space shuttle provides a new environment for material processing. The possibility of growing crystals by the floating-zone method in space has been explored in recent years. One of the important topics of the study is the flow phenomena in the melting zone. The driving forces of the flow are the surface-tension gradients along the free surface, the buoyancy force, and the electromagnetic force from the induction heating coil. The melt flow has direct effects on the heat and mass transfer in the crystal growth. It has been reported that undesirable flows may cause striation and poor quality in the crystal [3]. In a low-gravity environment, the natural convection is reduced, but the other driving forces will still exist. In order to take full advantage of the new environment, the nature of the flows within the melt has to be well understood.

The primary interest of the present work is to investigate the flow caused by surface-tension gradients. Hence, the flow caused by the electromagnetic field is not studied. Several investigations have been made to study the surface-tension driven flows in simulated floating-zone configurations. They were summarized in [4]. Experimental studies were carried out under both 1-g and low-gravity conditions, [5] to [11]. The fluids used in those tests were methyl alcohol, FC-43, hexadecane, octadecane, silicon oil, and sodium nitrate. The length, L, and the diameter, D, of the floating-zones studies were less than 1 cm and the L to D ratios ranged from 0.5 to 1. Most of the tests imposed a constant temperature difference between the top and the bottom rods. This kind of arrangement approximately simulates half of the floating-zone, which means the region from the heater to the top or the bottom rods, Fig. 1. All the tests, both under 1-g and low-g, observed thermocapillary flows in the melt and transition from steady axisymmetrical vortex flows to oscillatory flows, as the Marangoni number exceeded a critical value, which usually is of the order of magnitude of 10^4. Most of the results are qualitative observations. Very little quantitative results were obtained for the temperature and flow field distributions, because it is difficult to measure those quantities in small floating-zones on earth, let alone under low-gravity conditions in a sounding rocket. Numerical experiments are one way to obtain more quantitative information to understand the details of the surface-tension flows.

The early numerical studies of floating-zones were done in [12] and [13]. The flows were solved for a full floating-zone configuration with radiant-ring heating around the mid-plane of the zone. The range of parameters considered in thos papers is many orders of magnitude lower than those for actual silicon growth conditions. Therefore, more numerical work is needed to determine the details of floating-zone thermo-capillary flows.

In the present study, a finite difference method is used to solve the axisymmetric flow and temperature fields in a half floating-zone configuration. The main interest of this study is centered on the effects of Marangoni number, Ma, surface-tension Reynolds number, Re_s, and Prandtl number, Pr, on the surface-tension driven flow under weightless conditions. Other effects such as buoyancy, surface heat loss, and aspect ratio, A, (L/R), are also studied briefly. The range of

the parameters studied are: Ma from 1 to 10^5, Re_s from 0.01 to 10^7, Gr 0, 10^3, and 10^7, Pr from 0.01 to 100, and A 1 and 2. For a silicon floating-zone of 10 cm diameter, the range of Ma from 10 to 10^5 is equivalent to a surface temperature difference of 5.9 to 10^{-4} to 60°C. In actual silicon floating-zone crystal growth, the temperature difference along the surface is about 10 to 40°C ([7] and [12]). Thus, the parameter range studied herein covers the actual silicon crystal growth situation.

For each case studied, the vorticity, stream function, velocity, and temperature distributions are obtained. In order to facilitate the interpretation of the results, the solutions are displayed graphically in the form of constant-value contours. In order to obtain the solutions under the large ranges of Ma and Re_s, a strongly coupled nonlinear numerical scheme and variable grid size are employed. These schemes are capable of providing numerically stable solutions for large Marangoni number and surface-tension Reynolds number.

MATHEMATICAL FORMULATION

The floating-zone configuration to be studied is shown in Fig. 2. The flow is assumed to be axisymmetric and incompressible. The distribution of impurities and dopants, which usually exist in the melt, will not be considered herein because the main objective is to investigate the thermocapillary flow. Thus, the basic equations are those that express the conservation of mass, momentum, and energy.
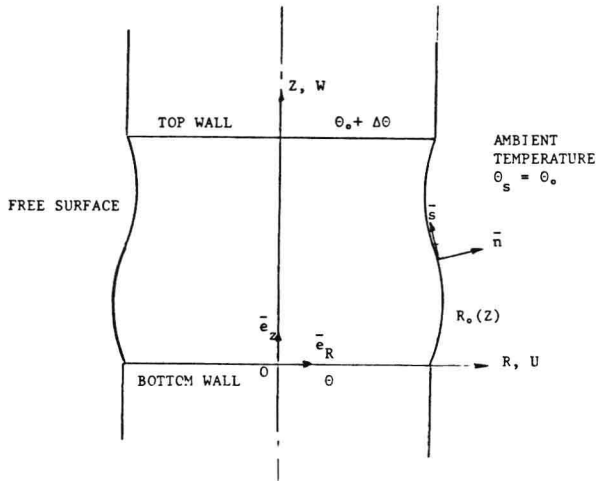

Figure 2 Floating zone coordinates

The boundary conditions are very complicated and involve the unknown solid-melt interface location, the temperature distribution in the solid, and the electro-magnetic flux distribution. Some simplifications are made to expedite the present work. The boundary conditions employed in the experimental work [5] to [11] are adopted here. Each of the two rods is maintained at a constant temperature so that a constant temperature difference is imposed on the liquid zone. Since the upper rod is taken to be hotter than the lower the fluid at the free surface will flow from the top to the bottom. This simulates the flow in the region from the heating coil to either of the rods and, thus, is referred to as a half floating-zone. The solid-melt boundary is assumed to be rigid and flat which is close to a properly controlled crystal growth situation. The melt surface is assumed to be cylindrical. This is justified in [14] for low-gravity conditions and small capillary numbers and verified by the results. The effect of the zone movement on the flow boundary conditions is also shown to be negligible in [14].

The dimensionless equations that describe the flows are:

$$\frac{\partial \Omega}{\partial t} + \frac{1}{r}\frac{\partial \psi}{\partial z}\frac{\partial \Omega}{\partial r} - \frac{1}{r}\frac{\partial \psi}{\partial r}\frac{\partial \Omega}{\partial z} - \frac{u\Omega}{r}$$

$$= \frac{1}{Re_s}\left\{ A^2 \frac{\partial}{\partial r}\left[\frac{1}{r}\left(\frac{\partial}{\partial r} r\Omega\right)\right] + \frac{\partial^2 \Omega}{\partial z^2} \right\} - \frac{Gr}{Re_s^2}\frac{\partial T}{\partial r} \qquad (1)$$

$$\frac{\partial T}{\partial t} + \frac{1}{r}\frac{\partial \psi}{\partial z}\frac{\partial T}{\partial r} - \frac{1}{r}\frac{\partial \psi}{\partial r}\frac{\partial T}{\partial z}$$

$$= \frac{1}{Ma}\left[\frac{A^2}{r}\frac{\partial}{\partial r}\left(r\frac{\partial T}{\partial r}\right) + \frac{\partial^2 T}{\partial z^2} \right] \qquad (2)$$

where the vorticity, Ω is

$$\Omega = \frac{1}{A^2 r}\frac{\partial^2 \psi}{\partial z^2} - \frac{\partial}{\partial r}\left[\frac{1}{r}\frac{\partial \psi}{\partial r}\right] \qquad (3)$$

In addition to the boundary conditions stated above a heat flux balance is specified at the free surface. In dimensionless variables the boundary conditions are:

$$\psi = 0, \quad \Omega = \frac{2\psi(r,0+\Delta z)}{\Delta z^2 r}, \quad T = 0 \text{ at } z = 0$$

$$\psi = 0, \quad \Omega = 0, \quad \frac{\partial t}{\partial r} = 0 \text{ at } r = 0$$

$$\psi = 0, \quad \Omega = \frac{2\psi(r,1-\Delta z)}{\Delta z^2 r}, \quad T = 1 \text{ at } z = 1$$

$$\psi = 0, \quad \Omega = \frac{\partial T}{\partial z}, \quad \frac{\partial T}{\partial r} = -Nu\, T \text{ at } r = 1$$

3

The surface-tension Reynolds number indicates the relative importance of inertia and viscous forces, the Marangoni number indicates the relative importance of convection and conduction, and relative importance of buoyancy to surface-tension gradient force is indicated by Gr/Re_s^2.

Numerical Scheme

The basic equations (1) to (3) are solved in an integral form by using an up-wind finite difference formulation introduced in [15]. The buoyancy term is included to study the effect of the Grashof number. After formulation, the non-linear finite difference equations are solved in a strong coupled form by the Newton-Raphson method. Non-uniform grid sizes are used to treat the regions where large gradients are expected. Details are given in Ref. 14.

RESULTS AND DISCUSSION

Most of the cases investigated are for unit aspect ratio, a constant Nusselt number of 0.3, and Gr = 0. The value of the Nusselt number will be justified later. Other cases with different aspect ratios, Nusselt numbers, and Grashof numbers were also studied. The parametric ranges covered and important results are listed in Table 1 for all the cases considered.

Table 1

The Conditions and Results for all Numerical Solutions

Ma	Re_s	Pr	Nu	Gr	A	Ω_{max}	Ω_{min}	$-\psi_{min}$ ×10^{+2}	ψ_{max} ×10^{+2}	$-\omega_{min}$ ×10^{+2}	$+\omega_{max}$ ×10^{+2}	$-\omega_{min}$ ×10^{+2}
10	10^{-1}	100	0.3	0	1	1.49	0.954	1.04	4.28	4.12	4.11	11.7
10^2	1	100	0.3	0	1	1.63	1.01	0.878	3.50	3.60	3.47	9.72
10^3	10	100	0.3	0	1	4.51	1.48	0.428	2.31	2.15	1.72	5.09
10^4	10^2	100	0.3	0	1	6.52	1.37	0.180	1.86	1.86	0.871	2.75
10^5	10^3	100	0.3	0	1	14.2	1.39	0.196	1.22	0.939	0.647	2.47
10	1	10	0.3	0	1	1.49	0.955	1.04	4.28	4.12	4.11	11.7
10^2	10	10	0.3	0	1	1.63	1.00	0.878	3.52	3.79	3.47	9.72
10^3	10^2	10	0.3	0	1	4.53	1.48	0.425	2.34	2.14	1.72	5.12
10^4	10^3	10	0.3	0	1	6.63	1.47	0.154	1.87	0.867	0.586	2.51
10^5	10^4	10	0.3	0	1	11.8	1.99	0.0767	1.30	0.559	0.969	2.76
10	10^2	0.1	0.3	0	1	1.50	0.885	1.02	4.04	4.19	4.01	11.5
10^2	10^3	0.1	0.3	0	1	1.56	1.43	0.724	2.50	4.25	2.98	8.47
10^3	10^4	0.1	0.3	0	1	3.68	1.62	0.316	1.13	2.44	1.44	3.79
10^4	10^5	0.1	0.3	0	1	3.24	0.785	0.166	0.771	1.26	0.896	1.69
10^5	10^6	0.1	0.3	0	1	3.06	0.317	0.0619	0.491	0.580	0.513	0.721
10	10^3	0.01	0.3	0	1	1.51	1.29	0.812	2.80	4.58	3.37	9.51
10^2	10^4	0.01	0.3	0	1	1.44	1.02	0.376	1.29	3.00	1.74	4.76
10^3	10^5	0.01	0.3	0	1	3.04	0.984	0.192	0.965	1.58	1.11	1.76
10^4	10^6	0.01	0.3	0	1	5.28	0.405	0.105	0.667	0.736	0.693	0.876
10^5	10^7	0.01	0.3	0	1	5.39	0.265	0.0733	0.489	0.483	0.484	0.611
10	1	10	0.3	0	2	2.22	1.16	2.44	15.1	10.5	16.6	20.3
10^2	10	10	0.3	0	2	2.15	1.09	2.03	18.2	10.6	14.0	16.4
10^3	10^2	10	0.3	0	2	3.76	1.21	0.975	8.99	6.49	6.33	10.9
10^4	10^3	10	0.3	0	2	10.84	1.67	0.361	5.83	2.28	1.98	9.06
10^5	10^4	10	0.3	0	2	16.06	0.995	0.628	4.22	3.03	3.51	6.12
10	10^3	0.01	0.3	0	2	2.24	1.01	2.09	11.8	12.7	12.3	17.6
10^2	10^4	0.01	0.3	0	2	2.19	1.76	1.20	6.90	12.3	7.47	10.3
10^3	10^5	0.01	0.3	0	2	4.05	1.13	0.804	7.57	8.19	6.03	8.15
10^4	10^6	0.01	0.3	0	2	8.71	0.719	0.523	5.16	5.16	3.92	4.00
10^5	10^7	0.01	0.3	0	2	15.0	0.553	0.395	5.92	5.92	2.96	3.01
10^4	10^3	10	0.03	0	2	6.22	1.31	0.180	1.30	0.864	0.596	2.57
10^4	10^3	10	3	0	1	6.24	1.66	0.269	1.97	0.959	1.07	3.64
10^4	10^5	0.01	0.03	0	1	3.59	0.398	0.105	0.653	0.723	0.679	0.854
10^4	10^5	0.01	3	0	1	3.59	0.441	0.116	0.733	0.810	0.756	0.979
10^4	10^3	10	0.3	10^3	1	6.45	1.35	0.142	1.31	0.878	0.570	2.54
10^4	10^6	0.01	0.3	10^7	1	5.13	0.336	0.0631	0.447	0.586	0.513	0.600

The Effects of Re_s, Ma, and Pr

All the cases discussed in this section are with A = 1, Nu = 0.3 and Gr = 0.

Prandtl number greater than unity

Figures 3 to 7 show the vorticity, isotherms, streamlines, axial velocity, and radial velocity contours for the flow with Pr = 10, and Ma = 10 to 10^5, i.e., Re_s = 1 to 10^4.

The difference between the minimum and the maximum of the numerical solution is divided into a number of equal-spaced intervals, ten for the temperature and stream function, and twenty for the vorticity, radial velocity, and axial velocity. The contours are plotted for every other division, starting at the lowest interval. The right boundary of the floating-zone configuration, Fig. 3, is the free surface, the left is the center line, and the top and the bottom correspond to the top and the bottom walls. The vorticity contours have the maximum positive value at the free surface, and the minimum negative value at the walls. The radial velocity contours form two cells due to the different flow directions. The lower core has the minimum negative velocity, and the upper core has the maximum positive velocity. The axial velocity contours have a negative minimum at the free surface. The axial velocity becomes positive on the other side of the core, and reaches a positive maximum near the middle of the floating-zone. Table 1 gives the minimum and maximum values for all the cases studied.

In general, the flow pattern is a clockwise, single-cell flow. The fluid moves from the top to the bottom along the free surface because the surface-tension decreases as temperature increases. From the energy equation, Eq. (2), it can be seen that the larger the Ma, the stronger is the convection. In Fig. 3, for Ma = 10, the isotherm pattern is a stratified conduction-type. No thermal convection effects can be observed. The linear temperature distribution along the free surface, Figs. 3 and 8, generates a uniform surface-tension gradient, which drives the fluid adjacent to the free surface. In terms of vorticity, the uniform surface-tension gradient creates an almost constant vorticity source along the free surface.

Because Re_s is small, the vorticity distribution is governed by diffusion. Without convection the vorticity contours are symmetrical with respect to the middle plane, z = 0.5, Fig. 3. Hence, the core of the flow cell is located at the middle plane, z = 0.5, and r = 0.83, Fig. 3. The radial velocity contours, Fig. 3, show a top to bottom symmetrical distribution. The axial velocity contours show a downward flow near the free surface that occupies a narrow region near the free surface, about one-fifth of the radius, and the upward flow occupies the rest of the region. The maximum downward velocity is 2.85 times higher than that of the upward flow, Table 1. When Ma increases to 100, Fig. 4, the stratified isotherms are displaced in the flow direction due to thermal convection. The free surface temperature becomes less linear, Fig. 8. The vorticity contours still show a diffusion dominant pattern, Fig. 4, because Re_s is small, 10. The flow field and the free-surface velocity distribution, Figs. 4 and 9, show little change from that of Ma = 10.
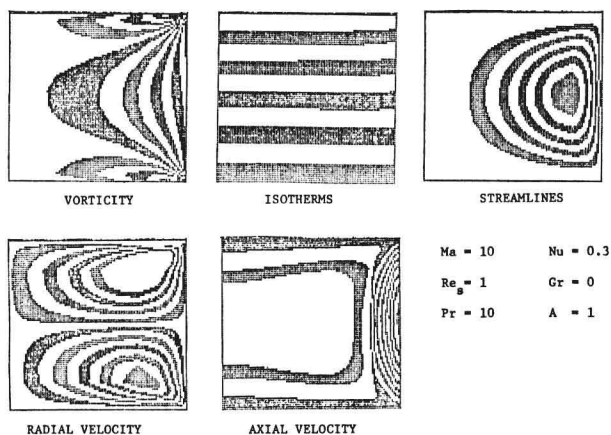
4

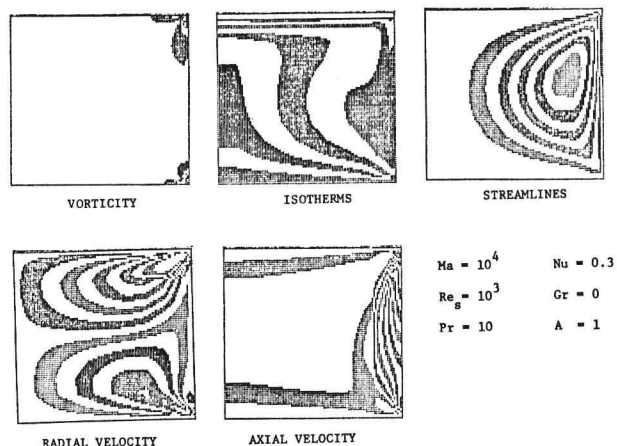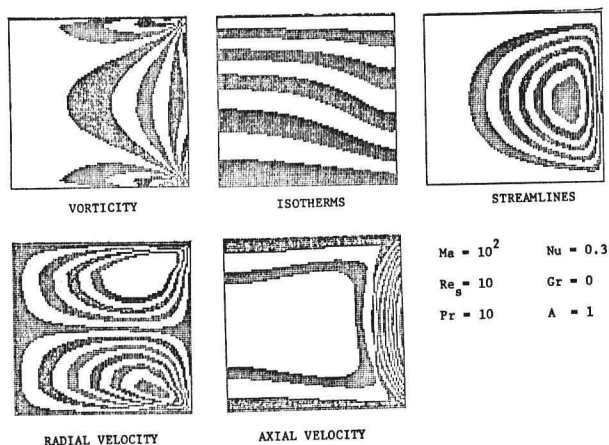Figure 3 Flow field contour

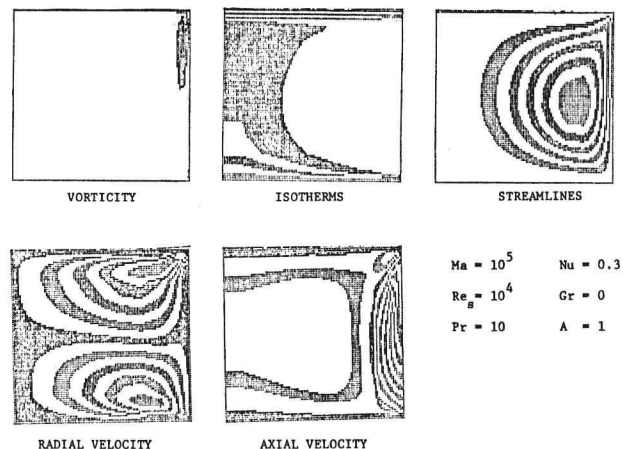Figure 6 Flow field contour

Figure 4 Flow field contour
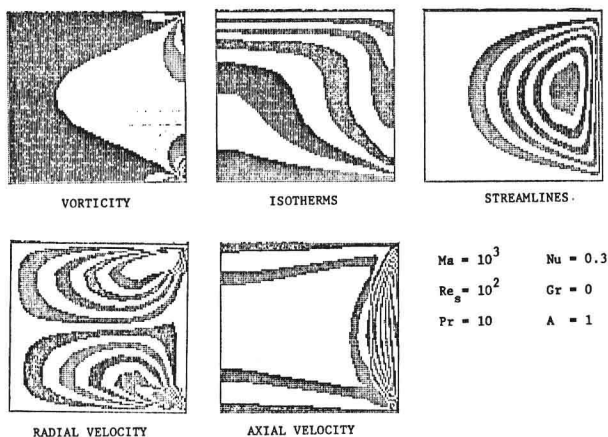

Figure 7 Flow field contour

Figure 5 Flow field contour

For $Ma > 10^3$, Figs. 5 to 7, the thermal convection becomes dominant over most of the floating-zone. The flow brings colder fluid toward the upper corner and displaces hot fluid towards the lower corner. The free-surface temperature distributions for $Ma = 10^4$ and 10^5, Fig. 8, indicate thermal boundary layers near the two rigid surfaces joined by an essentially uniform temperature region. In Fig. 6, $Re_s = 10^3$, the Re_s, or the vorticity convection, is not sufficiently large to influence the vorticity diffusion. Hence, the large vorticity sources created by the top and the bottom thermal boundary layers diffuse into the field, and accelerate the fluid locally. There is no significant driving force in the flat temperature zone so that velocity peaks occur near the two ends of the zone along the free surface, Fig. 9. The flow-cell core, Fig. 6, is located above the mid-plane of the floating-zone. This is because the thermal boundary layer is thicker at the upper corner. The flow phenomena in Fig. 6 have been seen in movies made by Chun and Schwabe.

5

In Fig. 7, because of the high Re_s, 10^4, the convection of vorticity becomes important and, as a result, the vorticity at the upper corner is moved downward by the flow and it does not diffuse into the interior as far as it does for smaller Re_s. The core of the flow cell is thus displaced downward. Fig. 10 shows the vorticity distribution across the line z = 0.54. For low Re_s, the distributions of the vorticity have a diffusion profile-high values occur at the free surface. As Re_s increases to 100, the convective effect starts to smooth out the vorticity gradient near the surface. When $Re_s = 10^4$, the vorticity at the free surface is much lower than at the adjacent interior. This high internal vorticity comes from upstream. The vorticity created by the surface-temperature gradient at the lower corner is confined to a small region by the flow. Hence, no local maximum of the surface velocity is observed, Fig. 9.

All the descriptions made above for $Pr = 10$ apply for $Pr = 100$ except for the case of $Ma = 10^5$ and $Re_s = 10^3$, Fig. 11. Because the Re_s is not sufficiently large to make the vorticity convection dominant, there are still two velocity peaks and the core of the flow cell is near the upper corner.
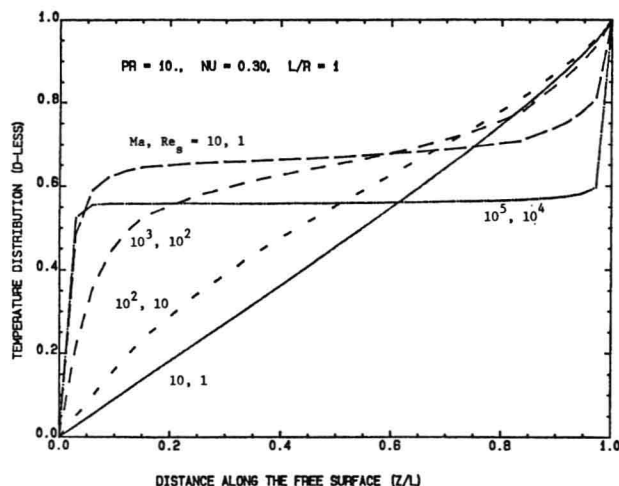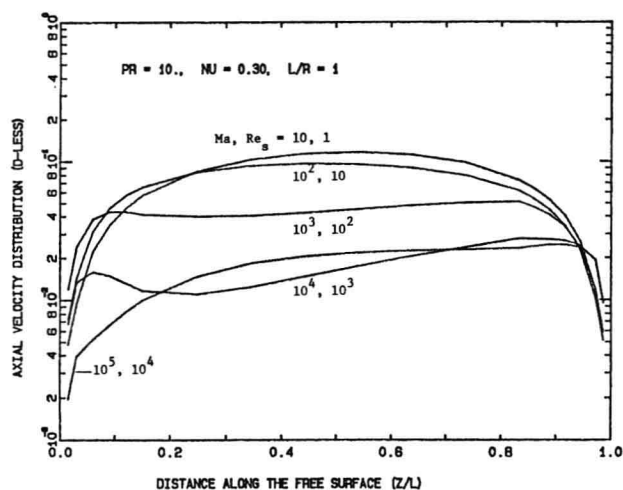
From the calculations for $Pr > 1$, it appears that the flow pattern changes qualitatively at a value of Re_s between 10^3 and 10^4. The major change in the thermal field occurs at a Ma somewhat larger than 10^3.

Prandtl number smaller than unity
    Figs. 12 to 16 show the flow fields for $Pr = 0.01$, $Ma = 10$ to 10^5, and $Re_s = 10^3$ to 10^7. The Ma has a similar effect on the isotherms as in the previous $Pr > 1$ cases. For $Pr < 1$, Re_s is always larger than Ma, that is, the vorticity convection occurs before the thermal convection. In Fig. 12, $Ma = 10$ and $Re_s = 10^3$, the vorticity contours indicate the convection effect, whereas the isotherms do not. In Fig. 12 and 13, the convection of vorticity causes a higher vorticity region near the lower corner. As a result, the cores of the flow cells are located in the lower half of the field, and the radial velocity is higher there. For $Re_s \geq 10^5$, Fig. 14 to 16, the strong convection of vorticity tends to homogenize the vorticity in the floating-zone. Therefore, the cores of the flow cells move back to the center of the field. Because of the vorticity convection effect, there are no peaks in free surface velocity.
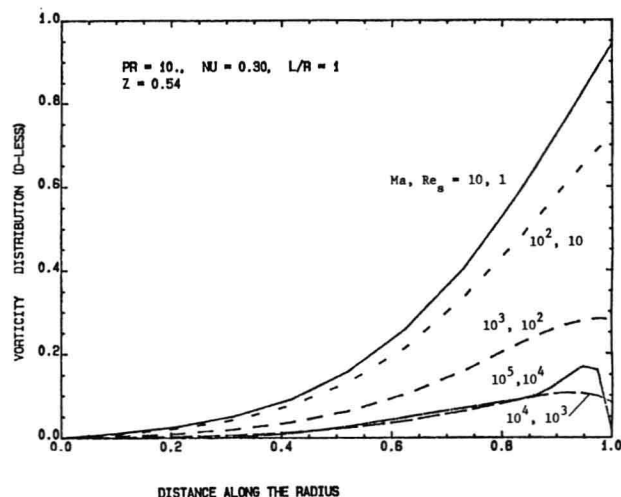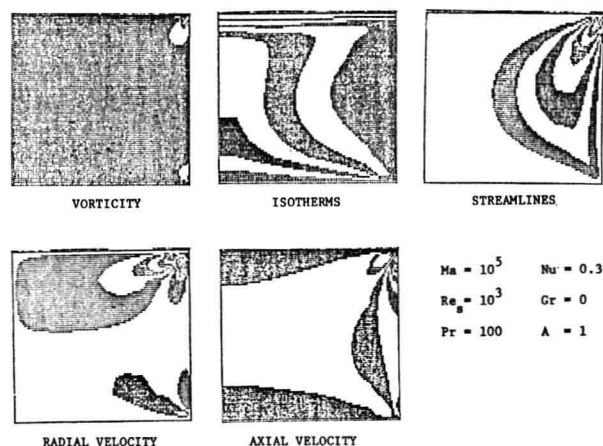

Figure 8 Free surface temperature profiles

Figure 10 Vorticity distributions

Figure 9 Free surface velocity profiles

Figure 11 Flow field contours

6

此为试读，需要完整PDF请访问：www.ertongbook.com

Effects of Nusselt number

The heat loss at the free surface increases with the Nusselt number. All cases to this point were computed for Nu = 0.3. In order to study the effect of surface heat loss, calculations were made for Ma = 10^4, Pr = 10 and 0.01, and Nu = 3 and 0.03. All aspects for Nu = 0.03 are found to be similar to those for Nu = 0.3. However, there are significant changes when Nu = 3. The surface temperature is much lower for Nu = 3. The temperature gradients at the top and in the middle of the free surface increase whereas it decreases at the bottom due to the higher heat loss. As a result the core of the flow is lower and the two velocity peaks are reduced.

Thus, it is seen that increasing the free-surface heat loss influences the flow much more than decreasing it. This is because the thermal convection in the zone overwhelms the heat loss when Nu ≤ 0.3. However, when Nu = 3 the heat loss is sufficiently strong to alter the temperature distribution established by thermal convection. This indicates that the surface heat loss will have larger effects on low Ma flows, in which thermal convection is relatively smaller.
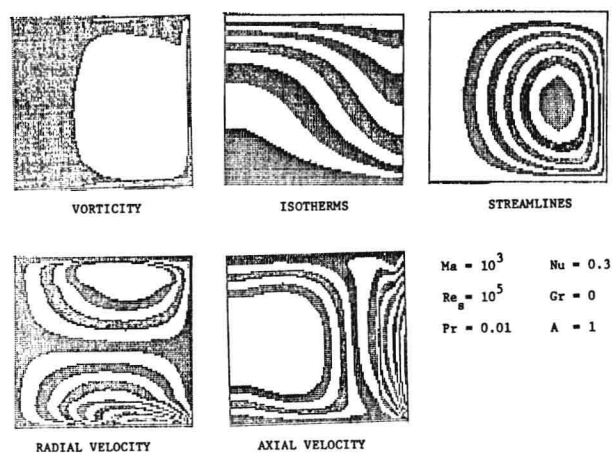
Figure 14 Flow field contours

$Ma = 10^3$ $Nu = 0.3$
$Re_s = 10^5$ $Gr = 0$
$Pr = 0.01$ $A = 1$
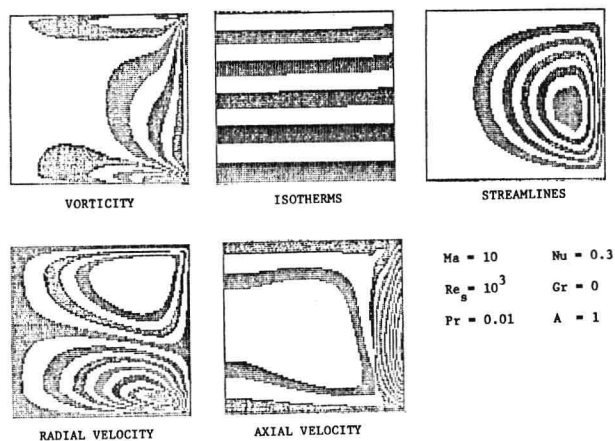
Figure 12 Flow field contours

$Ma = 10$ $Nu = 0.3$
$Re_s = 10^3$ $Gr = 0$
$Pr = 0.01$ $A = 1$
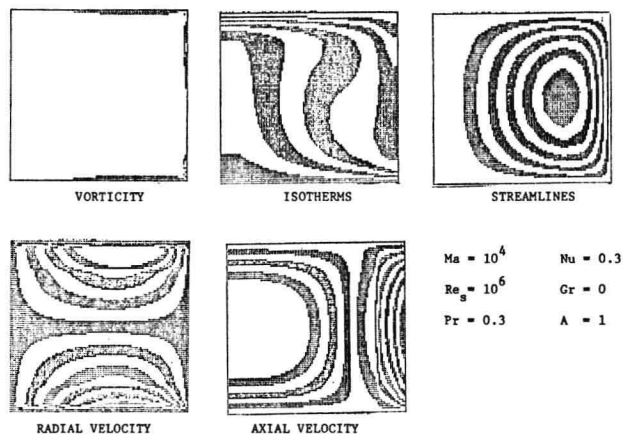
Figure 15 Flow field contours

$Ma = 10^4$ $Nu = 0.3$
$Re_s = 10^6$ $Gr = 0$
$Pr = 0.3$ $A = 1$
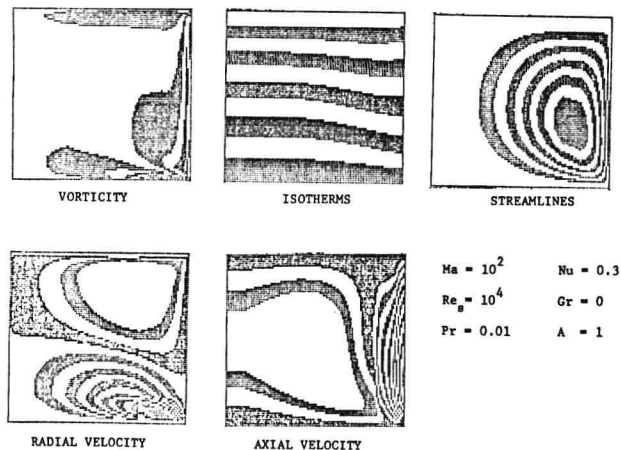
Figure 13 Flow field contours

$Ma = 10^2$ $Nu = 0.3$
$Re_s = 10^4$ $Gr = 0$
$Pr = 0.01$ $A = 1$

Figure 16 Flow field contours

$Ma = 10^5$ $Nu = 0.3$
$Re_s = 10^7$ $Gr = 0$
$Pr = 0.01$ $A = 1$

7

From the movies of Chun and Schwabe two velocities can be observed at about Ma = 10^4. This seems to imply that the actual Nusselt number is around 0.3 or less. In order to obtain more detailed information on Nu a solution is obtained for the interaction between the melt and its surroundings (air). The streamlines and isotherms are shown in Fig. 17. The thermal boundary condition imposed on the fr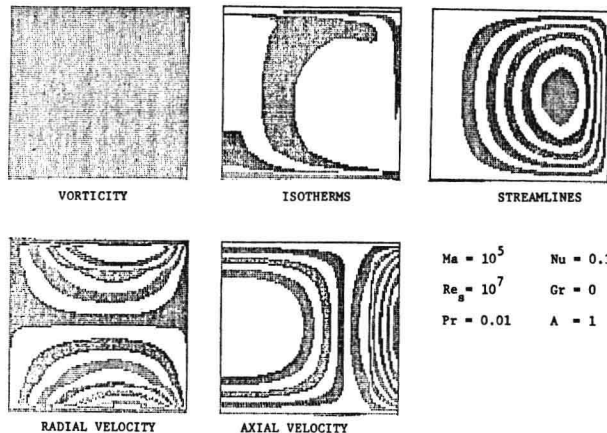ee surface is the continuity of temperature in the melt and in the air. Thus, the heat transfer from the melt to the air is determined from the solution. The conditions for the melt are taken to be the experimental conditions in (9). The width of the air annulus is the same as the melt radius and its height is twice that of the melt. The surface temperature of the air annulus is taken to be that of the lower zone surface temperature. The patterns are similar to those previously computed and the average Nusselt number is found to be 0.184. Thus, the value used in the parametric studies seems appropriate.

For Pr < 1, such as in silicon growth, the heat transfer will be higher than in the low-temperature experiments because of radiation losses. Nu = 0.3 is equivalent to a heat transfer coefficient of 0.019 watt/$^{\circ}$C/cm^2, which is in the neighborhood of the actual value for a silicon rod with a 10 cm diameter.
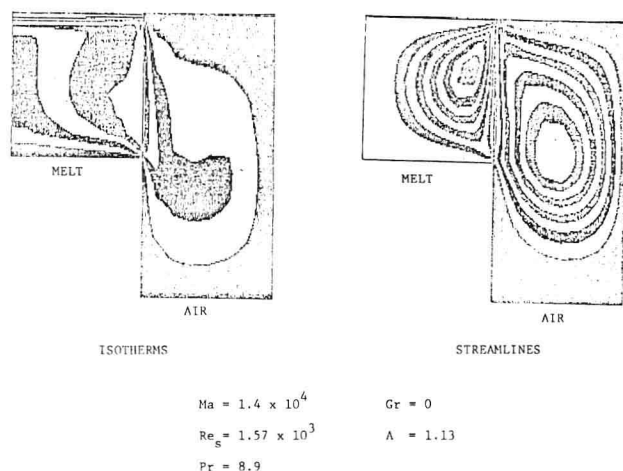

Ma = 1.4×10^4 Gr = 0

Re$_s$= 1.57×10^3 A = 1.13

Pr = 8.9

Figure 17 Isotherms and streamlines for air-melt configuration with zero air surface temperature

SUMMARY

All the solutions show a single-cell streamline pattern with the core located at about three-quarters of the radius away from the axis. The downward axial velocity near the free surface is about two to four times higher than the upward axial velocity near the axis.

The Marangoni number determines the relative importance of thermal convection to thermal diffusion. For Ma $\leq$ 10, the isotherms from a conduction pattern. When Ma reaches 10^4, thermal boundary layers are formed along the top wall and along the top and bottom of the free surface convection. A near zero temperature gradient region falls in between the two thermal boundary layers along the free surface.

The surface-tension Reynolds number determines the relative importance of the vorticity convection to the vorticity diffusion. When Re$_s$ < 10, the vorticity is distributed by diffusion. When $\overline{Re}_s$ reaches 10^4, convection confines the vorticity diffusion to the region close to its source.

The combined effects of vorticity and thermal convection cause a shift of the location of the core of the flow cell and the shape change in the streamlines.

There are significant differences between the flow with Pr > 1 and Pr < 1, such as the streamline patterns, and two peak surface velocities appear in the flow with Pr > 1 and do not in the flow with Pr < 1.

The flow patterns for aspect ratios of one and two are similar. No multiple cells were found.

The effect of heat loss on the flow is small when the Nusselt number is less than 0.3 and Ma = 10^4, because the thermal convection in the fluid is much stronger than the heat loss. The Nusselt number will have greater effects on low Marangoni number flows.

The buoyancy force generates negative vorticity in most of the flow field. The negative vorticity weakens the positive vorticity generated from the surface, hence, reduces the flow.

Space limitations prelude detailed discussions of the effects of the aspect ratio, the Grashof number, and other factor, but these are presented in detail in (14).

REFERENCES

1. Pimputkar, S.M., Ostrach, S. 1981. Convective Effects in Crystal Growth from Melt, J. Crystal Growth. 55, 614-646.

2. Keller, W., and Muhlbauer, A., 1981. Floating-Zone Silicon, Marcel Dekker, Inc., New York and Basel.

3. Vanek, P., Kadeckovas, 1979. Growth Striation in Fe 3 Wt % Si Single Crystals Grown by Floating Zone Melting at Various Growth Rates. J. of Crystal Growth, 47. 458-462.

4. Ostrach, S. 1982. Low-Gravity Fluid Flows, Ann. Rev. Fluid Mech. 14, 313-345.

5. Vargas, M., Ostrach, S., Kamotani, Y., 1982. Surface Tension Driven Convection in a Simulated Floating-Zone Configuration. Rep. FTAS/TR-82-159, Dept. of Mech. and Aero. Eng., Case Western Reserve University, Cleveland, Ohio.

6. Chun, Ch.-H., 1980. Experiments on Steady and Oscillatory Temperature Distribution in a Floating-Zone Due to the Marangoni Convection, Acta Astronautica 7, 479-88.

7. Chun. Ch.-H., 1980. Marangoni Convection in a Floating-Zone Under Reduced Gravity, J. of Crystal Growth, 45, 600-610.

8. Chun, Ch.-H., Wuest, W., 1979. Experiments on the Transition from the Steady to the Oscillatory Maragoni-Convection of a Floating-Zone Under Reduced Gravity Effect. Acta Astronautica 5, 1073-82.

9. Schwabe, D., Preiser, F., Scharmann, A., 1981. Verification of the Oscillatory State of Thermo-capillary Convection in a Floating-Zone Under Low Gravity. Physikalisches Institut der Justins-Liebig-Universitat, Heinrich-Buff-Ring 1b, D-6300, Glessen, West Germany.

10. Schwabe, D., Scharmann, A., 1979. Some Evidence for the Existence and Magnitude of a Critical Marangoni Number for the Onset of Oscillatory Flow in Crystal Growth Melt. J. Crystal Growth, 46, 125-31.

11. Schwabe, D., Scharmann, A., Preiser, F., 1978. Experiments on Surface Tension Driven Flow in Floating-Zone Melting. J. Crystal Growth 43, 305-12.

12. Chang, C.E., Wilcox, W.R., 1976. Analysis of Surface Tension Driven Flow in Floating-Zone Melting. Int. J. Heat Mass Transfer, 19, 335-66.

13. Clark, P.A., Wilcox, W.R., 1980. Influence of Gravity on Thermocapillary Convection in Floating-Zone Melting of Silicon. J. Crystal Growth, 50, 460-69.

14. Fu, B.-I and Ostrach, S., 1983. Numerical Solutions of Floating-Zone Crystal Growth, Case Western Reserve University, Department of Mechanical and Aerospace Engineering, FTAS/TR-82-169, 1983.

15. Gosman, A.D., Pun, W.M., Runchal, A.K., and Spalding, D.B., 1969. Heat and Mass Transfer in Recirculating Flows. Academic Press, London.

CONVECTIVELY INDUCED CRYSTAL-MELT INSTABILITIES—
INFLUENCE OF GRAVITY AND ROTATION

M. E. Glicksman, Q. T. Fang
Materials Engineering Department
Rensselaer Polytechnic Institute
Troy, New York

S. R. Coriell, G. B. McFadden, and R. F. Boisvert
National Bureau of Standards
Washington, DC

ABSTRACT

The stability of the crystal-melt interface
surrounding a vertical, coaxial melt annulus undergoing
stable convection flow was investigated. A novel in-
stability, designated as "coupled mode", was found due
to the effect of convection on the deformable crystal-
melt interface. This instability occurs above a
cricital Grashof number of circa 160, which is an order
of magnitude smaller than that corresponding to a rigid-
wall interface. At instability, the crystal-melt inter-
face was found to rotate with a period ranging from a
few minutes to more than ten hours depending on the
melt radial gap. The scalings were fully characterized
both in a linear stability analysis and in an experi-
ment with a general agreement between them.

BACKGROUND

Previous experiments conducted by Mickalonis and
Glicksman [1,2] disclosed a novel interface instability
under thermal conditions for which the crystal-melt
interface is supposed to be morphologically stable in
the absence of flow. The present study [3] was
carried out to characterize this instability in detail,
both experimentally and theoretically.

Our primary interest evolves on the fact that such
convective instabilities depend directly on the gravi-
tational acceleration, g, through the Grashof number
$Gr = g\beta\Delta TL^3/\nu^2$, where β is the volumetric expansion
coefficient of the melt, ΔT is the temperature drop
across the melt gap, $\bar{L}$, and ν is the kinematic viscos-
ity. Thus, gravity has a direct influence on the
occurrence of such instabilities, and may be used to
modify their appearance through the scaling laws
implicit in the Grashof numbers. A large reduction in
the value of g, for example, in a low earth orbit
$g = 10^{-4}g_e$, where $g_{e\cdot} = 980$ cm/sec^2, would permit a
modest increase in the length scale $\bar{L}$, by more than an
order of magnitude.

The control of fluid motions and their influence on
the crystal morphology is a central theme of materials
processing in space. By investigating flow interaction
with solid-liquid interfaces one can establish the
sensitivity of the crystallization process and its
ultimate outcome to the gravitational conditions pre-
vailing during processing. It was for this purpose that
the experimental and theoretical studies outlined in this
paper were carried out.

EXPERIMENTAL

In this experiment, a long cylindrical sample of
pure succinonitrile (Prandtl number of melt = 22.8) was
heated by an electrical current passed through a fine,
coaxial, vertical wire, and the outer radius of the
crystal was maintained at a constant temperature below
the melting point, so that a vertical melt annulus
formed between the coaxial heating wire and the
surrounding crystal-melt interface. With this arrange-
ment the temperature decreases monotonically from the
liquid toward the solid across the solid-liquid inter-
face, and consequently the interface would be morpholog-
ically stable in the absence of fluid flow. However,
the presence of convection flow in this experiment in-
duces a novel interface instability under certain
critical conditions. The critical condition for the
occurrence of this interface instability is governed by
the Grashof number (ratio of buoyance to viscous forces).
The state associated with the formation of the unstable
interface is designated as the "helical mode". The
presence of this mode occurs only when the Grashof
number is larger than a certain critical value. Since
this mode would not occur in the absence of either
fluid flow or the crystal-melt interface, it is thus
also denoted as the "coupled mode". At smaller Grashof
numbers, the interface is configured as a straight,
stationary cylindrical shape. This state is referred to
as the "cylindrical mode". The morphology of these two
states is shown in Figure 1a and 1b.

STATUS OF THEORY

These experimental discoveries motivated a com-
panion theoretical investigation by S.R. Coriell, et
al., [4] at the National Bureau of Standards. They used
linear perturbation analysis of the Navier-Stokes
equation for small Reynolds number in the Boussinesq
approximation but included boundary conditions pertinent
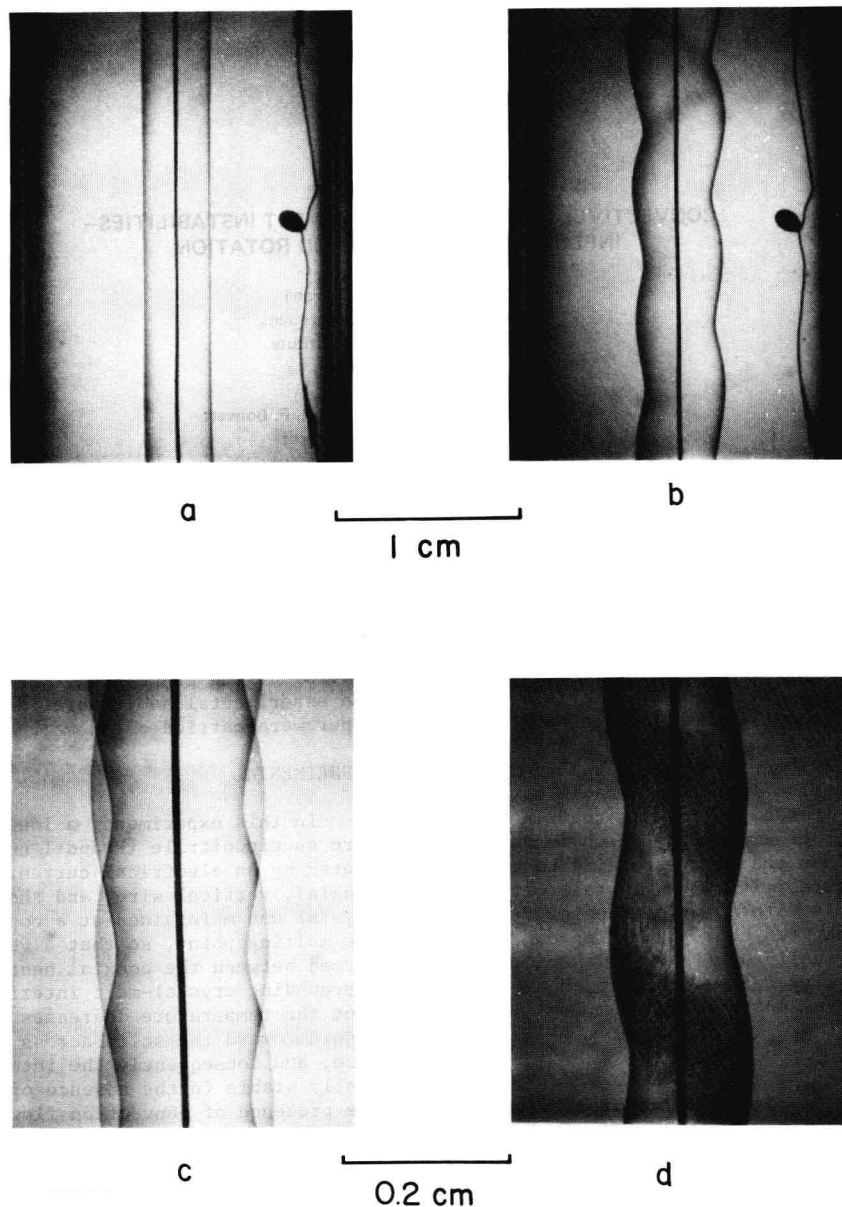to the crystal-melt interface, which are different from

Figure 1. A long cylindrical sample of succinonitrile is heated by an electrical current through a coaxial vertical wire so that a vertical melt annulus forms between the wire and the surrounding crystal-melt interface. a) below a critical Grashof number of circa 160, the crystal-melt interface is cylindrical; b) above the critical Grashof number, a helical crystal-melt interface forms; c) multiple exposures show motion of the helical interface; and d) a dendritic "belt" formed by abrupt undercooling indicates the helicity of the interface.

those associated with a rigid wall. The Grashof numbers calculated for neutral stability from this theory as a function of the spatial frequency of the perturbation is shown in Figure 2. The higher axisymmetric mode (n=0) in the figure is essentially identical to that obtained previously by Choi and Korpela [5] for rigid iso-thermal boundaries. In contrast, the lower axi-symmetric mode and the asymmetric mode (n=1) only occur when a crystal-melt interface is present (see Fig. 2). This theory has predicted that the onset of instability

by an asymmetric mode at a Grashof number of 176, which is in good agreement with our experiments.

SUMMARY OF RESULTS

The results from these experiments and a general comparison with the theoretical calculations is summarized in the following:

1) A non-axisymmetric mode, designated earlier as

12